Energy Engineering

Tech Science Press

http://doi.org/10.32604/ee.2026.085812

ARTICLE

Heavy-Load Start-Up Compensation for an IPMSM-Driven Gravity Energy Storage Hoisting Unit

Zheng Cao, Wei Li* and Teng Li

School of Automation and Electrical Engineering, Lanzhou University of Technology, Lanzhou, China
*Corresponding Author: Wei Li. Email: 252085406065@lut.edu.cn

Received: 19 May 2026; Accepted: 08 July 2026; Published: 12 November 2026

ABSTRACT: The hoisting unit is a key electromechanical energy-conversion component in a hoisting-based gravity energy storage system (GESS). Under heavy-load start-up conditions, an interior permanent magnet synchronous motor (IPMSM)-driven hoisting unit may suffer from start-up rollback, delayed torque buildup, and low-speed current fluctuation, which reduce start-up reliability. This paper develops a torque-balance-based adaptive gravity feedforward (AGF) compensation framework for improving the heavy-load start-up performance of an IPMSM-driven GESS hoisting unit. An electromechanically coupled model is established to describe the interaction among the IPMSM drive, transmission mechanism, inclined load, and nonlinear friction. Based on the model, the proposed AGF provides physically matched feedforward compensation for the dominant start-up disturbances while retaining the conventional cascaded feedback structure. Comparative simulations are conducted under conventional proportional-integral (PI) control, fixed feedforward, basic AGF, and improved AGF. Under the 4.8 t full-load condition, conventional PI control produces a maximum start-up rollback of approximately 9.1 mm, while fixed feedforward reduces it to approximately 6.1 mm but introduces a pronounced transient current peak. The improved AGF further reduces the maximum rollback to approximately 0.1 mm and improves low-speed current smoothness. Under the 2.4 t half-load condition, adaptive gravity reconstruction avoids fixed-feedforward overcompensation. Simulations with the motor rotor inertia varied by ±20% around its nominal value show that the proposed strategy retains satisfactory start-up performance under moderate plant-side rotor-inertia variation. The proposed framework provides a practical control approach for improving the heavy-load start-up reliability of IPMSM-driven GESS hoisting equipment without changing the basic hardware topology.

KEYWORDS: Gravity energy storage system (GESS); IPMSM drive; hoisting unit; heavy-load start-up; adaptive gravity feedforward (AGF)

1 Introduction

Gravity energy storage systems (GESSs) have attracted increasing attention as a potential solution for large-scale and long-duration energy storage because of their long service life, low life-cycle cost, and suitability for terrain-based energy conversion applications [1–3].

Recent studies on modular gravity energy storage and GESS management have further indicated that system structure, energy management, and power-stability control are important issues for practical GESS operation [4–6]. In a hoisting-based GESS configuration, electrical energy and gravitational potential energy are converted through the lifting and lowering motion of a heavy load. Therefore, the hoisting unit acts as a key electromechanical energy-conversion component of the storage system. Interior permanent magnet synchronous motors (IPMSMs) are suitable for compact heavy-load drive units because of their high torque

Copyright © 2027 The Authors. Published by Tech Science Press. This work is licensed under a Creative Commons Attribution 4.0 International License, which permits unrestricted use, distribution, and reproduction in any medium, provided the original work is properly cited.

density, high efficiency, and favorable dynamic performance [7,8]. However, under an extreme suspended condition with a steep slope and a heavy load, the start-up transient of an IPMSM-driven GESS hoisting unit is difficult to control accurately. Start-up rollback, delayed torque buildup, and low-speed current fluctuation may directly affect the start-up reliability and operational stability of GESS hoisting equipment.

During heavy-load start-up, conventional cascaded proportional-integral (PI) control mainly relies on speed-error feedback. Since the gravity load is already present at the initial instant, the electromagnetic torque may not be established rapidly enough, leading to reverse displacement before stable lifting is achieved [9]. In addition, zero-speed friction switching, load variation, and equivalent-inertia uncertainty further complicate the start-up transient. A fixed gravity feedforward torque can reduce part of the static gravity disturbance under a given load, but it may cause undercompensation at full load or overcompensation at half load. Therefore, a compensation method consistent with the physical torque balance of the hoisting unit is required.

Disturbance observers (DOBs) and sliding mode control (SMC) have been widely studied for motor-drive and motion-control systems [10,11]. Recent PMSM studies have also introduced current-constrained and observer-based nonlinear control to improve transient current regulation and disturbance rejection [12,13]. However, these methods may increase computational burden and parameter-tuning difficulty, and chattering in SMC may be undesirable for heavy-load mechanical transmission systems [14]. For a GESS hoisting unit, the dominant start-up disturbances, including gravity load, zero-speed nonlinear friction, and inertia-related transients, are partly predictable from physical parameters. Model-derived feedforward compensation is therefore a practical way to reduce the feedback burden while preserving the conventional cascaded control structure. Accordingly, the comparative analysis is organized around progressively enhanced feedforward strategies within this common control framework, allowing the respective contributions of gravity reconstruction, friction regularization, and inertia-feedforward clamping to be evaluated without introducing differences in feedback architecture.

This paper investigates the heavy-load start-up transient of an IPMSM-driven GESS hoisting unit from the viewpoint of electromechanical energy-conversion equipment reliability. An electromechanically coupled model is established to describe the torque interaction among the IPMSM drive, gearbox transmission, drum mechanism, inclined heavy load, and nonlinear friction. Based on the torque-balance relationship of this model, an improved adaptive gravity feedforward (AGF) strategy is developed to reconstruct the gravity compensation baseline, regularize the zero-speed friction term, and suppress unnecessary inertia-feedforward injection in the low-speed region. The present study focuses on the start-up transient from the suspended condition to upward hoisting. Regenerative lowering, reverse operation, and transitions between motoring and generating modes involve different power-flow directions and control objectives, and therefore require further investigation within a bidirectional operation framework.

The main contributions of this paper are summarized as follows:

1. An electromechanically coupled model is established for the IPMSM-driven GESS hoisting unit to describe the torque interaction among the motor drive, transmission mechanism, inclined heavy load, and nonlinear friction.
2. A model-derived AGF compensation framework is developed to reduce the initial torque deficit during heavy-load start-up by coordinating gravity-load reconstruction, zero-speed friction regularization, and low-speed inertia-feedforward clamping.
3. Comparative simulations covering full-load and half-load operation, fixed feedforward, basic AGF, improved AGF, and parameter-sensitivity cases are conducted to evaluate start-up rollback suppression, low-speed current smoothness, variable-load adaptability, and parameter sensitivity.

The remainder of this paper is organized as follows. Section 2 establishes the electromechanically coupled model of the GESS hoisting unit. Section 3 presents the improved AGF feedforward–feedback control strategy and its digital implementation. Section 4 reports the simulation results and engineering evaluation. Section 5 concludes the paper.

2 Electromechanically Coupled Modeling of the GESS Hoisting Unit

2.1 Load Dynamics of the Heavy-Load Hoisting System

Fig. 1 shows the electromechanical energy-conversion configuration of the IPMSM-driven GESS hoisting unit considered in this study.

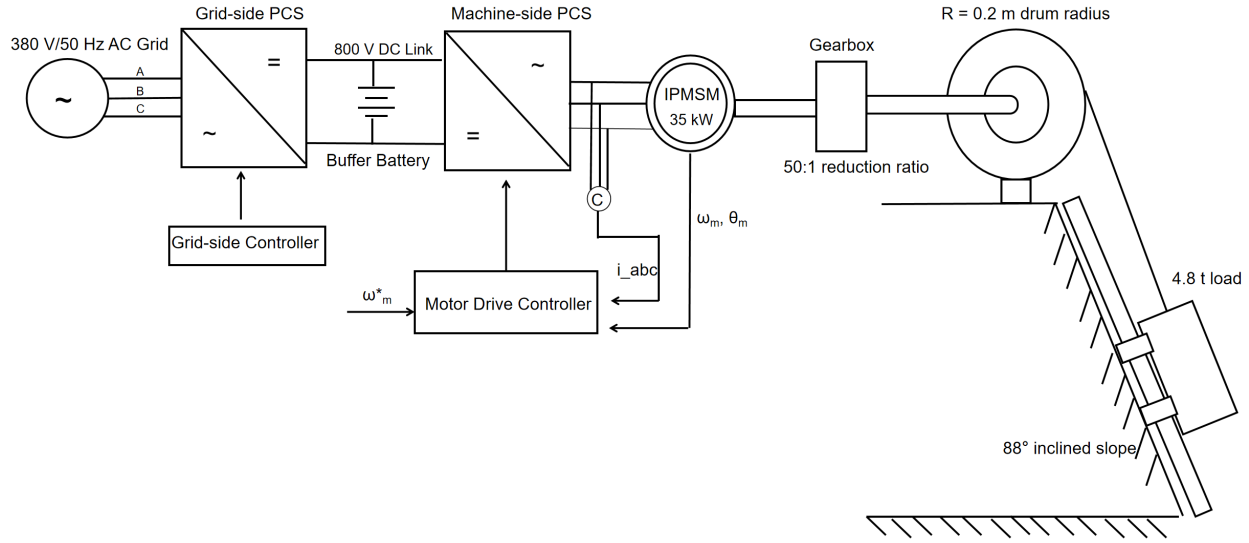


Figure 1: Electromechanical configuration of the IPMSM-driven GESS hoisting unit under the extreme suspended full-load condition.

The system consists of a 380 V/50 Hz AC grid, grid-side and machine-side power conversion systems (PCSs), an 800 V DC link with a buffer battery, an interior permanent magnet synchronous motor (IPMSM), a gearbox, a drum mechanism, and an inclined hoisting mechanism. The illustrated condition corresponds to the extreme suspended full-load start-up case with a 4.8 t load and an 88° inclined track. Since the DC-link voltage is maintained by the grid-side PCS and buffer battery, the machine-side model is used to analyze the torque balance during heavy-load start-up.

The motor-side mechanical motion equation is written as

$$J_{eq}\frac{d\omega_m}{dt} = T_{em} - T_{load} - B_m\omega_m - T_f(\omega_m), \tag{1}$$

where J_{eq} is the equivalent total inertia referred to the motor shaft, ω_m is the motor mechanical angular speed, T_{em} is the electromagnetic torque, B_m is the equivalent viscous-friction coefficient referred to the motor shaft, T_{load} is the gravity-load torque referred to the motor side, and $T_f(\omega_m)$ is the nonlinear friction torque excluding the linear viscous-friction component.

In the simulation model, B_m represents the lumped viscous-friction effect of the motor– transmission–load system. The separate rotor viscous-damping coefficient in the IPMSM block is set to $B_r = 0$, while the load-side translational viscous-friction coefficient is $c_v = 1000\ \mathrm{N \cdot s/m}$. Using the kinematic relationship

$v = R\omega_m/i$, the equivalent coefficient referred to the motor shaft is calculated as $B_m = B_r + c_v(R/i)^2 = 0.016\ \mathrm{N \cdot m \cdot s/rad}$.

The equivalent inertia is expressed as

$$J_{eq} = J_m + J_{tr} + \frac{J_d + mR^2}{i^2}, \tag{2}$$

where J_m is the motor rotor inertia, J_{tr} is the equivalent transmission inertia on the motor side, J_d is the drum-side rotational inertia, and mR^2/i^2 is the translational load inertia reflected to the motor shaft. In the nominal simulation setting, J_{eq} is represented by the equivalent total inertia listed in Table 1, consistent with the mechanical components defined in Eq. (2).

Table 1: Electrical and mechanical parameters of the IPMSM-driven GESS hoisting unit.

Parameter	Value	Unit
Electrical parameters		
DC-link bus voltage (V_{nom})	800	V
Stator d-/q-axis inductance (L_d/L_q)	0.244/0.298	mH
Stator phase resistance (R_s)	3.0	mΩ
Permanent-magnet flux linkage (ψ_m)	0.0437	Wb
Number of pole pairs (p)	8	–
Mechanical parameters		
Full-load/Half-load mass (m)	4800/2400	kg
Equivalent total inertia at motor shaft (J_{eq})	0.2002	kg·m^2
Equivalent viscous-friction coefficient at motor shaft (B_m)	0.016	N·m·s/rad
Reduction gear ratio (i)	50	–
Hoist drum radius (R)	0.2	m
Total transmission efficiency (η)	0.90	–
Breakaway static friction torque (T_{st})	6.2	N·m
Coulomb friction torque (T_c)	5.0	N·m
Stribeck characteristic speed (ω_s)	1.0	rad/s
Stribeck shape factor (δ)	2.0	–

Under the suspended condition with slope angle θ and load mass m, the steady-state gravity-load torque referred to the motor side is

$$T_{load} = \frac{mgR\sin\theta}{i \cdot \eta}, \tag{3}$$

where g is the gravitational acceleration, R is the hoist drum radius, i is the gearbox reduction ratio, and η is the overall transmission efficiency. Here, T_{load} denotes the physical gravity-induced resisting torque reflected to the motor shaft, with η accounting for the transmission efficiency. It constitutes the dominant resisting torque during heavy-load start-up.

The nonlinear mechanical friction is described by the Stribeck model:

$$T_f(\omega_m) = \left[T_c + (T_{st} - T_c)e^{-|\omega_m/\omega_s|^\delta}\right]\mathrm{sgn}(\omega_m), \tag{4}$$

where T_c is the Coulomb friction torque, T_{st} is the breakaway static friction torque, ω_s is the Stribeck characteristic speed, and δ is the shape factor. The discontinuity of $\mathrm{sgn}(\omega_m)$ at zero speed may cause abrupt friction-torque switching, which is regularized in the subsequent feedforward design.

2.2 Electrical Dynamics and Torque Generation of the IPMSM

Under the extreme suspended start-up condition, the IPMSM provides the supporting electromagnetic torque against the gravity-load torque and nonlinear friction. In the synchronous rotating d–q reference frame, the stator voltage equations are expressed as

$$\begin{cases} u_d = R_s i_d + L_d \dfrac{di_d}{dt} - \omega_e L_q i_q, \\ u_q = R_s i_q + L_q \dfrac{di_q}{dt} + \omega_e L_d i_d + \omega_e \psi_m, \end{cases} \tag{5}$$

where u_d and u_q are the d- and q-axis stator voltages, i_d and i_q are the corresponding stator currents, R_s is the stator resistance, L_d and L_q are the stator inductances, $\omega_e = p\omega_m$ is the electrical angular speed, p is the number of pole pairs, and ψ_m is the permanent-magnet flux linkage.

The electromagnetic torque is given by

$$T_{em} = \frac{3}{2} p \left[\psi_m i_q + (L_d - L_q) i_d i_q \right]. \tag{6}$$

Rotor field-oriented control with $i_d^* = 0$ is adopted. Thus, the torque-current relationship used for the feedforward–feedback control channel is simplified as

$$T_{em} = K_t i_q, \qquad K_t = \frac{3}{2} p \psi_m, \tag{7}$$

where K_t is the equivalent torque coefficient. The reference torque is converted into the target q-axis current command by

$$i_q^* = \frac{T_{ref}^*}{K_t}. \tag{8}$$

Together with the mechanical motion equation in Eq. (1), Eqs. (5)–(8) describe the electromechanical coupling between load-side torque demand and motor-side current response. Under conventional cascaded proportional-integral (PI) control, the compensating electromagnetic torque is established only after a speed deviation and current response appear. Since the gravity-load torque already acts at the initial instant of heavy-load start-up, the transient torque balance may satisfy

$$T_{em} < T_{load} + T_f(\omega_m) \;\Rightarrow\; J_{eq} \frac{d\omega_m}{dt} < 0. \tag{9}$$

This torque deficit is the physical cause of start-up rollback and motivates the model-derived feedforward compensation strategy developed in Section 3.

3 Improved AGF Feedforward–Feedback Control Strategy

Based on the electromechanically coupled model established in Section 2, a torque-balance-based adaptive gravity feedforward (AGF) framework is developed for the heavy-load start-up transient of the

GESS hoisting unit. The purpose is to provide anticipatory torque compensation before large speed deviation and reverse displacement occur.

The proposed AGF is inserted in parallel with the conventional cascaded PI loop. The feedforward path compensates the main model-derived start-up torque demand, while the feedback loop corrects residual modeling errors, parameter uncertainty, and unmodeled disturbances. This structure reduces the initial burden on the speed-loop controller without changing the basic hardware topology of the IPMSM-driven GESS hoisting unit.

The coordinated design of the improved AGF is based on the physical composition of the heavy-load start-up torque demand. The gravity-reconstruction term establishes a controller-side compensation baseline for the dominant static gravity-load torque according to the estimated load mass and local track slope. The friction-regularization term smooths the direction function used in the friction-feedforward branch, thereby mitigating abrupt switching of the friction-compensation torque around zero speed. The low-speed clamping function suppresses unnecessary acceleration-related inertia-feedforward injection near standstill and gradually restores the inertia compensation as the motor speed increases. Thus, the three components respectively address the dominant static gravity demand, zero-speed friction switching, and acceleration-related transient demand, forming a coordinated feedforward compensation strategy for heavy-load start-up.

3.1 Torque-Balance-Based Feedforward Components

This subsection formulates the main feedforward torque components used to construct the controller-side start-up torque reference.

3.1.1 Static Gravity Feedforward Compensation

During heavy-load start-up, the gravity-load torque is the dominant predictable resisting component. Based on the torque-balance relationship in Eq. (3), the controller-side gravity feedforward torque is reconstructed as

$$T_g = \frac{\hat{m} g R \sin \hat{\theta}}{i}, \tag{10}$$

where $\hat{m}$ is the estimated load mass, $\hat{\theta}$ is the estimated track slope angle, g is the gravitational acceleration, R is the hoist drum radius, and i is the gearbox reduction ratio. Here, "adaptive" denotes updating the gravity-compensation baseline according to the current load and slope information. The estimated load mass $\hat{m}$ may be obtained from supervisory loading records, weighing information, or load-identification measurements. In the present framework, $\hat{m}$ is supplied by the supervisory loading system, updated before each hoisting cycle or whenever the payload changes, and held constant during that cycle. The local track slope is obtained from a predefined track-profile map indexed by the measured load position, $\hat{\theta}(t) = \Theta\big(s(t)\big)$, where $s(t)$ is provided by a position sensor. Alternatively, the slope may be obtained from an inclination sensor or a suitable estimation method. Thus, $\hat{m}$ is updated on an operating-cycle or payload-change basis, whereas $\hat{\theta}$ is updated online according to the measured load position.

For the full-load condition with $m = 4800$ kg and $\theta = 88^{\circ}$, the nominal controller-side gravity baseline is

$$T_{g,0} = \frac{m g R \sin \theta}{i} \approx 188.2\ \mathrm{N \cdot m}. \tag{11}$$

For comparison, a fixed feedforward baseline is defined as

$$T_{FF,\text{fixed}} = T_{g,0} + \Delta T_b \approx 195\ \text{N}\cdot\text{m}, \tag{12}$$

where ΔT_b is a static bias term. This fixed value is tuned for the nominal full-load condition and remains unchanged when the load varies, which may lead to overcompensation under reduced-load conditions. By contrast, T_g and $T_{g,0}$ in Eqs. (10) and (11) are simplified controller-side baselines used to generate the gravity-feedforward command and are not intended to exactly reproduce the physical gravity-load torque T_{load} defined in Eq. (3). Accordingly, the transmission-efficiency term is not explicitly included in these baseline expressions, and any resulting mismatch is corrected by the feedback loop.

3.1.2 Inertia-Related Feedforward with Low-Speed Clamping

The inertia-related torque demand is introduced to compensate the acceleration component during start-up. Based on the controller-side estimate $\hat{J}_{eq}$ of the equivalent total inertia, the inertia-feedforward torque is formulated as

$$T_I = \gamma(\omega_m)\hat{J}_{eq}\alpha^*, \tag{13}$$

where $\hat{J}_{eq}$ is the controller-side estimate of the equivalent total inertia referred to the motor shaft, α^* is the commanded motor mechanical angular acceleration associated with the start-up speed reference, and $\gamma(\omega_m)$ is the low-speed clamping function. For the upward start-up simulations considered in this study, the motor-speed reference is generated by a discrete rate limiter. Starting from zero, the reference increases toward 346 rpm by 0.2306 rpm, equivalent to approximately 0.02415 rad/s, at each update with $T_r = 1$ ms. The commanded acceleration used in the inertia-feedforward term is calculated from two consecutive reference samples as

$$\alpha^*[n] = \frac{\omega_m^*[n] - \omega_m^*[n-1]}{T_r}.$$

Accordingly, $\alpha^* = 24.1484\ \text{rad/s}^2$ during the constant-ramp stage. The same start-up speed-reference profile and commanded-acceleration calculation are used in all simulation cases.

The clamping function is defined as

$$\gamma(\omega_m) = \begin{cases} 0, & |\omega_m| < \omega_{th}, \\ \dfrac{|\omega_m| - \omega_{th}}{\omega_{th}}, & \omega_{th} \le |\omega_m| < 2\omega_{th}, \\ 1, & |\omega_m| \ge 2\omega_{th}, \end{cases} \tag{14}$$

where ω_{th} is the prescribed low-speed threshold.

As shown in Fig. 2a, the inertia channel is disabled near zero speed, gradually restored in the transition region, and fully activated when $|\omega_m| \ge 2\omega_{th}$. In this study, $\omega_{\text{th}} = 1.047$ rad/s, corresponding to 10 rpm. In general, ω_{th} should be selected above the speed-measurement fluctuation range around standstill so that the inertia-feedforward term remains suppressed before reliable forward motion is established, but sufficiently low to avoid delaying the required inertia compensation during the subsequent acceleration stage. Its selection should therefore consider the low-speed measurement resolution and fluctuation as well as the start-up speed-reference profile. The value adopted in this study is selected according to the

low-speed measurement characteristics and start-up requirements of the investigated system, and may be adjusted accordingly for other hoisting units.

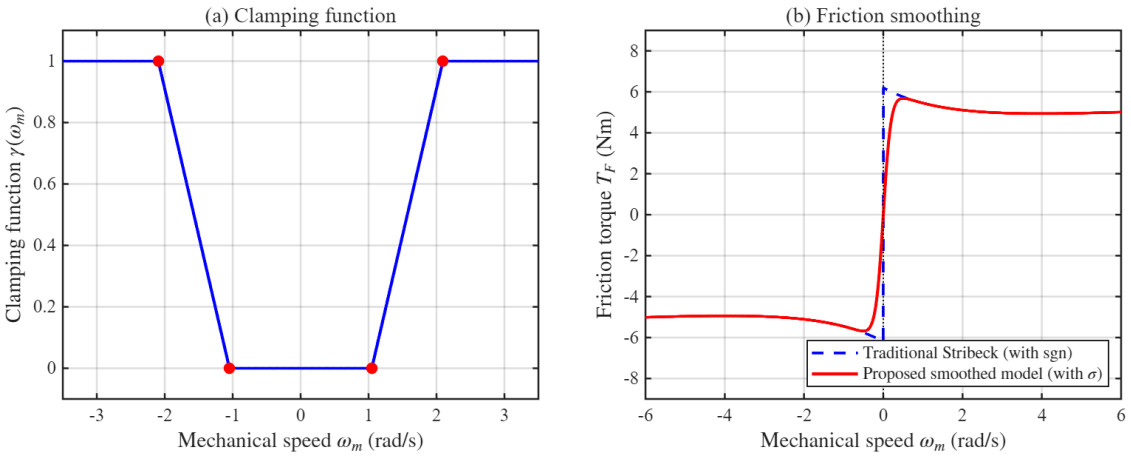


Figure 2: Key nonlinear characteristics used in the improved AGF strategy: (**a**) low-speed clamping function for inertia feedforward; (**b**) traditional and Sigmoid-smoothed friction torque characteristics.

3.2 Zero-Speed Friction Regularization

The sign function in the Stribeck friction model is discontinuous at zero speed, which may cause abrupt friction-torque switching and low-speed current fluctuation during heavy-load start-up [15–17]. To obtain a continuous friction compensation term, the direction function is regularized by a Sigmoid mapping [18]:

$$\sigma(\omega_m) = \frac{2}{1 + e^{-k\omega_m}} - 1, \tag{15}$$

where $k > 0$ is the smoothing factor.

The friction feedforward torque is then written as

$$T_F = \left[T_c + (T_{st} - T_c)e^{-|\omega_m/\omega_s|^\delta}\right]\sigma(\omega_m) = T_{str}(\omega_m)\sigma(\omega_m), \tag{16}$$

where T_c is the Coulomb friction torque, T_{st} is the breakaway static friction torque, ω_s is the Stribeck characteristic speed, δ is the shape factor, and $T_{str}(\omega_m)$ denotes the magnitude part of the Stribeck model.

As shown in Fig. 2b, the Sigmoid mapping provides a continuous transition around $\omega_m = 0$. The smoothing coefficient k determines the transition steepness of the regularized friction torque. For the adopted mapping,

$$\sigma(\omega_m) = \tanh\left(\frac{k\omega_m}{2}\right), \tag{17}$$

the maximum local slope occurs at $\omega_m = 0$ and is equal to $k/2$. For any finite positive k, the mapping remains continuous and bounded.

Fig. 3 shows that small values of k produce a wide transition region and slow friction-compensation buildup, whereas an excessively large value results in a steep variation near zero speed and increases sensitivity to low-speed fluctuations. Therefore, $k = 10$ was selected empirically as a compromise between compensation buildup speed and low-speed torque smoothness.

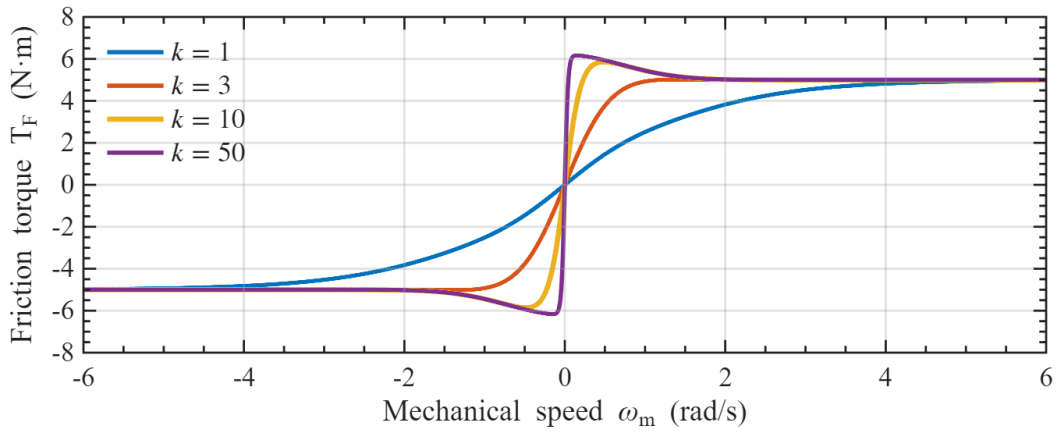


Figure 3: Calculated regularized friction-torque characteristics for different values of the smoothing coefficient k.

3.3 Composite Feedforward Torque and Digital Implementation

The gravity feedforward torque, inertia-related feedforward torque, and friction compensation torque are superposed as

$$T_{FF,\mathrm{raw}} = T_g + T_I + T_F. \tag{18}$$

To reduce high-frequency fluctuation in the feedforward path, a first-order digital low-pass filter is applied to $T_{FF,\mathrm{raw}}$. The filter is executed synchronously with the outer speed-control loop. Therefore, the sampling period is set to $T_s = T_{so} = 1$ ms, and the filtered feedforward torque is calculated as

$$T_{FF}(n) = b_0 T_{FF,\mathrm{raw}}(n) + b_1 T_{FF,\mathrm{raw}}(n-1) - a_1 T_{FF}(n-1), \tag{19}$$

where n is the control-period index. The filter coefficients obtained by Tustin discretization are [19]

$$b_0 = b_1 = \frac{\omega_c T_s}{2 + \omega_c T_s}, \qquad a_1 = \frac{\omega_c T_s - 2}{2 + \omega_c T_s}. \tag{20}$$

In the simulations, a nominal design cutoff frequency of $f_c = 200$ Hz is used. With $\omega_c = 2\pi f_c$ and $T_s = 1$ ms, the corresponding discrete-filter coefficients are

$$b_0 = b_1 \approx 0.3859, \qquad a_1 \approx -0.2283. \tag{21}$$

To quantify the phase lag introduced by the digital filter, its frequency response is expressed as

$$H\left(e^{j\Omega}\right) = \frac{b_0 + b_1 e^{-j\Omega}}{1 + a_1 e^{-j\Omega}}, \qquad \Omega = 2\pi f T_s, \tag{22}$$

where f is the frequency of the composite feedforward signal. The corresponding phase lag is

$$\phi(f) = \arg\left[H\left(e^{j2\pi f T_s}\right)\right], \tag{23}$$

and the frequency-dependent equivalent phase delay is calculated as

$$\tau_{\phi}(f) = -\frac{\phi(f)}{2\pi f}. \tag{24}$$

For the nominal 200 Hz filter, the calculated phase lags at 10, 20, 50, 100, and 200 Hz are approximately -2.86°, -5.72°, -14.15°, -27.35°, and -49.15°, respectively. The corresponding equivalent phase delays are approximately 0.795, 0.794, 0.786, 0.760, and 0.683 ms. These results indicate that the digital filter introduces a finite and frequency-dependent phase lag in the composite feedforward command. In general, the cutoff frequency f_c should be selected high enough to limit the phase delay in the start-up feedforward command, but low enough to attenuate high-frequency fluctuations and avoid an excessive discrete transient response. Its selection should be coordinated with the sampling period of the outer speed-control loop and evaluated through both frequency-domain phase-delay analysis and time-domain torque-buildup comparison. The cutoff-frequency comparison for the present system is provided in Section 4.6.

3.4 Overall Control Topology and Execution Logic

Fig. 4 shows the compact signal-flow topology of the improved AGF feedforward–feedback strategy. The topology is based on rotor field-oriented control of the IPMSM with $i_d^* = 0$, and the AGF path is connected in parallel with the speed-loop PI controller to provide start-up torque compensation.

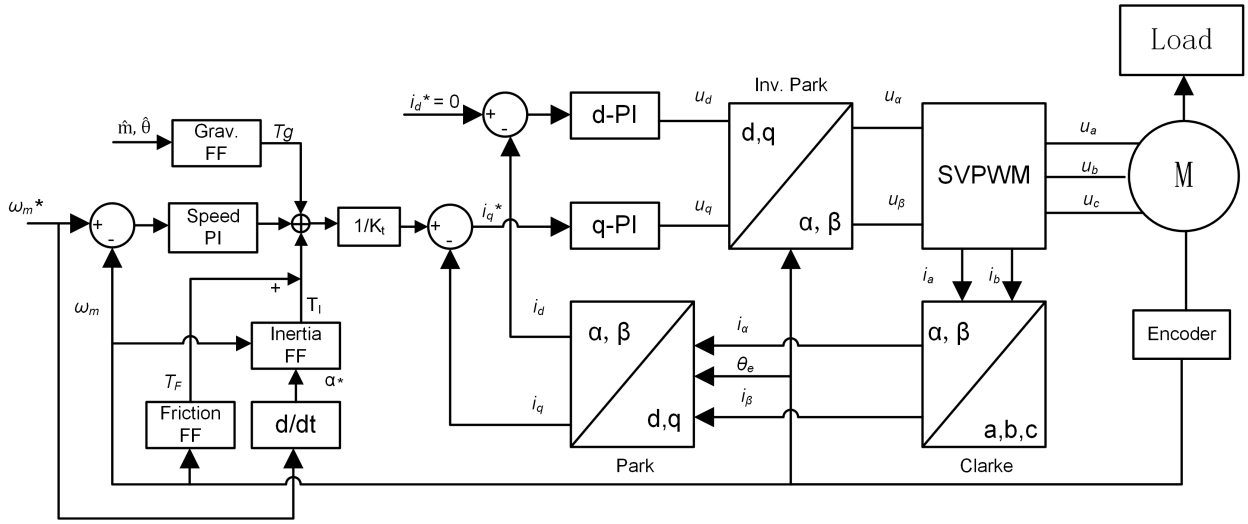


Figure 4: Compact signal-flow topology of the improved AGF feedforward–feedback strategy for the IPMSM-driven GESS hoisting unit.

As shown in Fig. 4, the feedforward path provides the composite torque command for the heavy-load start-up transient. The compact diagram represents the feedforward branch at the signal-flow level; in the digital implementation, the raw composite feedforward torque is processed by the discrete filter in Eq. (19) to obtain the effective feedforward torque T_{FF}. The final torque reference is then expressed as

$$T_{ref}^{*} = T_{PI}^{*} + T_{FF}, \tag{25}$$

where T_{PI}^{*} is the torque command generated by the speed-loop PI controller.

According to the torque-to-current relationship in Eq. (7), the target q-axis current command is calculated as

$$i_q^* = \frac{T_{ref}^*}{K_t}. \tag{26}$$

Together with $i_d^* = 0$, the current commands are processed by the inner current-loop PI regulators, coordinate transformations, and SVPWM modulation.

In this structure, the feedforward path provides anticipatory torque support before large speed deviation develops, while the feedback loop corrects residual modeling errors and unmodeled disturbances. Therefore, the proposed strategy improves the heavy-load start-up response without changing the basic hardware topology of the GESS hoisting unit.

4 Simulation Results and Engineering Evaluation

The main electrical, mechanical, and control parameters used in the simulations are listed in Tables 1 and 2. The simulation cases are designed to evaluate the heavy-load start-up reliability of the IPMSM-driven GESS hoisting unit, with emphasis on start-up rollback, phase-current smoothness, load adaptability, and parameter sensitivity.

Table 2: Control parameters used in the simulations.

Parameter	Value	Unit
Feedforward-compensation parameters		
Sigmoid mapping smoothness factor (k)	10	–
Low-speed clamping threshold (ω_{th}, 10 rpm)	1.047	rad/s
LPF cutoff frequency (f_c)	200	Hz
PI control parameters		
Inner current-loop sampling period (T_{si})	100	μs
Outer speed-loop sampling period (T_{so})	1	ms
d-axis current-loop PI gains ($K_{p,id}/K_{i,id}$)	0.8779/710.3004	–
q-axis current-loop PI gains ($K_{p,iq}/K_{i,iq}$)	1.0744/1061.5	–
Speed-loop PI gains ($K_{p,\omega}/K_{i,\omega}$)	1/50	–

All simulation cases use the same electromechanically coupled model, speed reference, sampling periods, and PI controller parameters. In the full-load and half-load load-adaptation comparison, the plant-side equivalent total inertia is kept at the nominal value listed in Table 1, while the load mass is varied in the gravity-load torque and gravity-feedforward reconstruction. The compared strategies differ only in the feedforward compensation path. The reported phase current represents the instantaneous inverter phase-current response during the start-up transient and is used to compare the relative electrical stress among different control strategies.

4.1 Benchmark Performance of Conventional Cascaded PI Control

The conventional cascaded PI controller is first tested under the extreme suspended full-load condition to provide a baseline for evaluating the proposed feedforward compensation strategy. The corresponding load displacement and phase-current responses are shown in Fig. 5.

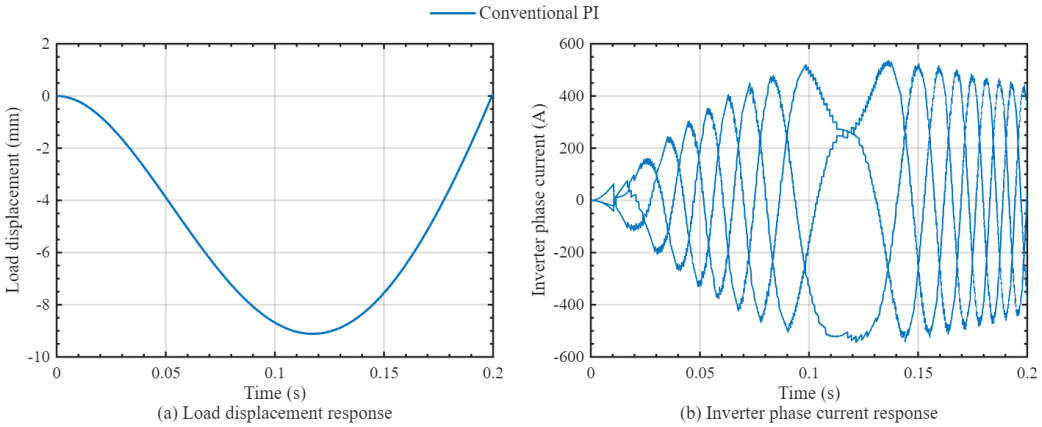


Figure 5: Benchmark performance of conventional cascaded PI control under the extreme suspended full-load condition ($m = 4800$ kg): (**a**) load displacement response; (**b**) phase-current response.

As shown in Fig. 5a, the conventional cascaded PI controller produces a clear start-up rollback, with the maximum rollback reaching 9.1124 mm near 0.12 s. Fig. 5b shows that the phase current builds up with a delay and exhibits transient fluctuation in the low-speed region. These results are consistent with the torque-deficit mechanism described in Eq. (9), indicating that speed-error feedback alone cannot establish the supporting electromagnetic torque rapidly enough under the suspended full-load start-up condition. Therefore, this case is used as the benchmark for the following AGF-based compensation comparisons.

4.2 Transient Limitation of Fixed Gravity Feedforward

To examine the effect of direct gravity compensation, a fixed feedforward baseline of $T_{FF,\mathrm{fixed}} = 195\ \mathrm{N \cdot m}$ is introduced under the extreme suspended full-load condition ($m = 4800$ kg). This value is slightly higher than the nominal controller-side gravity baseline $T_{g,0} \approx 188.2\ \mathrm{N \cdot m}$.

As shown in Fig. 6a, the fixed gravity feedforward reduces the maximum start-up rollback from 9.1124 mm to 6.138 mm, confirming that anticipatory gravity compensation can alleviate the initial torque deficit. However, the remaining rollback indicates that a constant feedforward term cannot fully handle low-speed friction variation and inertia-related transient demand.

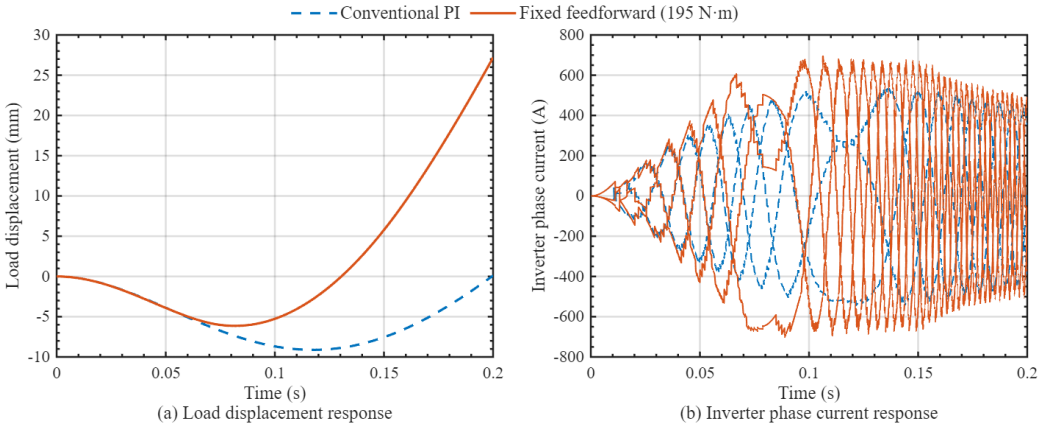


Figure 6: Comparison between conventional cascaded PI control and fixed gravity feedforward under the extreme suspended full-load condition: (**a**) load displacement response; (**b**) phase-current response.

Fig. 6b further reveals an electromechanical trade-off. Although fixed gravity feedforward improves the mechanical displacement response, it produces an instantaneous inverter output phase-current peak close to 700 A and intensifies the current oscillation during the initial low-speed stage. This peak is mainly caused by the direct application of the fixed gravity-feedforward torque at start-up, which results in a rapid increase in the torque command and the corresponding current reference during the establishment of the load-balancing electromagnetic torque. The resulting short-duration current surge increases the instantaneous current stress and may increase the conduction loss, switching loss, and thermal loading of the semiconductor switches.

4.3 Variable-Load Adaptability under the Half-Load Condition

To evaluate load adaptability, the fixed feedforward and the basic AGF are compared under the 2400 kg half-load condition. The basic AGF denotes gravity feedforward reconstructed from the current load mass and slope angle, without zero-speed friction regularization, low-speed inertia clamping, or discrete low-pass filtering.

As shown in Fig. 7a, the fixed feedforward torque of 195 N·m produces evident overcompensation under the reduced load, because this value is tuned for the 4.8 t full-load condition and remains unchanged when the load decreases. Although this excessive torque injection suppresses the apparent start-up rollback, it no longer matches the actual gravity-load demand of the 2400 kg condition and leads to an overly aggressive upward displacement response.

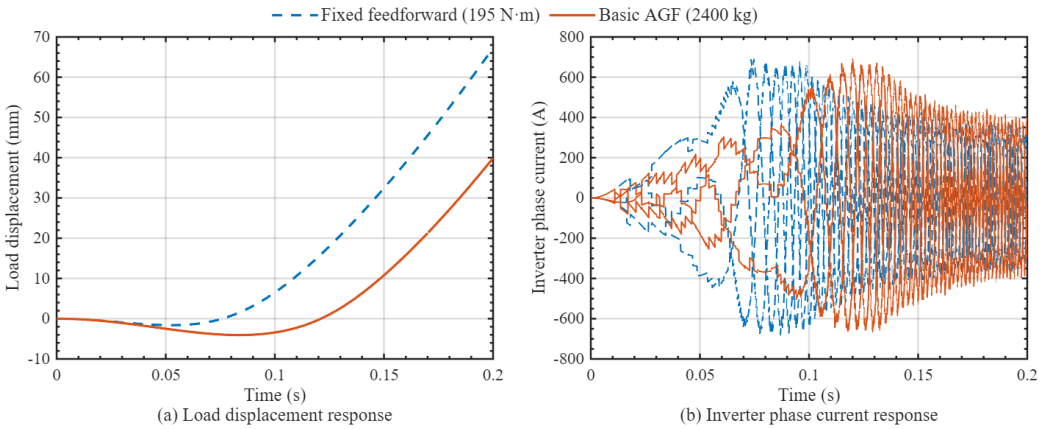


Figure 7: Comparison between fixed feedforward and the basic AGF under the half-load condition: (**a**) load displacement response; (**b**) phase-current response.

In contrast, the basic AGF updates the gravity compensation baseline according to the current mass and slope, thereby restoring a physically matched feedforward torque for the half-load condition. Because zero-speed friction and inertia-related transients are not yet compensated, a residual rollback of 4.0 mm still appears. However, Fig. 7b shows that the basic AGF mitigates the early current oscillation caused by fixed overcompensation, although low-speed current fluctuation remains. These results verify the variable-load adaptability of adaptive gravity reconstruction and indicate the need for further friction regularization and inertia-related compensation in the improved AGF design.

4.4 Full-Load Start-Up Performance of the Improved AGF

Fig. 8 compares the responses of the basic AGF and the improved AGF under the extreme suspended full-load condition (m = 4800 kg). The basic AGF only updates the gravity compensation baseline, whereas the improved AGF further introduces zero-speed friction regularization and inertia-related compensation.

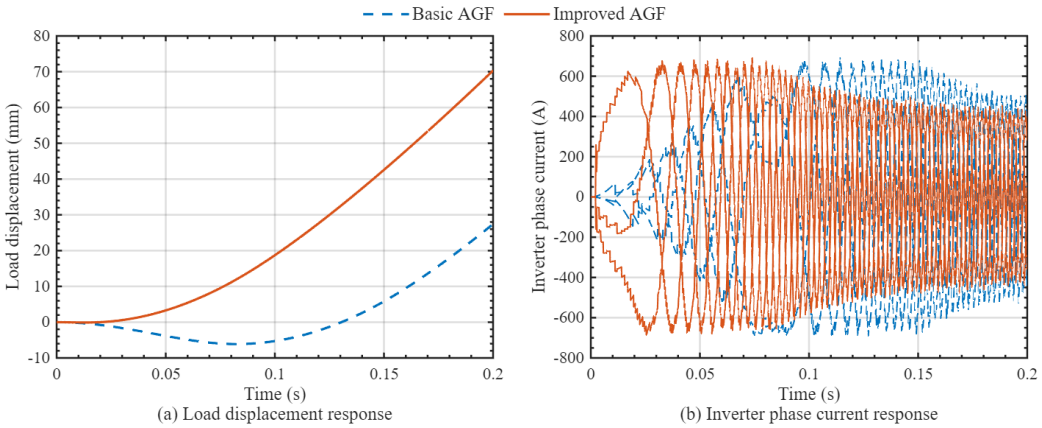


Figure 8: Comparison between the basic AGF and the improved AGF under the extreme suspended full-load condition: (**a**) load displacement response; (**b**) phase-current response.

As shown in Fig. 8a, the basic AGF produces a maximum rollback of 6.116 mm during heavy-load start-up, indicating that gravity-baseline reconstruction alone cannot sufficiently suppress the full-load rollback. In contrast, the improved AGF reduces the maximum rollback to 0.0894 mm and restores positive displacement much earlier.

Fig. 8b shows that the improved AGF produces a rapid current buildup at the initial stage. This response is required to establish the supporting electromagnetic torque under the suspended full-load condition and should not be regarded simply as an undesirable overshoot. Compared with the basic AGF, the improved AGF reduces irregular low-speed current fluctuation and allows the phase current to enter a stable periodic state earlier. These results show that the improved AGF provides stronger rollback suppression and a smoother low-speed current response under the extreme suspended full-load condition.

4.5 Torque Buildup and Parameter Sensitivity of the Improved AGF

To further explain the full-load start-up improvement, the electromagnetic-torque buildup and parameter sensitivity of the improved AGF are evaluated under the extreme suspended full-load condition.

As shown in Fig. 9, the electromagnetic torque is estimated from the q-axis current feedback according to Eq. (7). Under conventional cascaded PI control, the torque builds up slowly and remains below the static load demand during the early start-up stage, which corresponds to the torque-deficit condition in Eq. (9). In contrast, the improved AGF establishes the supporting torque much earlier and rapidly brings the response toward $T_{g,0}$, the nominal controller-side gravity-compensation baseline used for torque-buildup comparison, which differs from the physical gravity-induced resisting torque T_{load} referred to the motor shaft in Eq. (3). This explains the improved rollback suppression shown in Fig. 8.

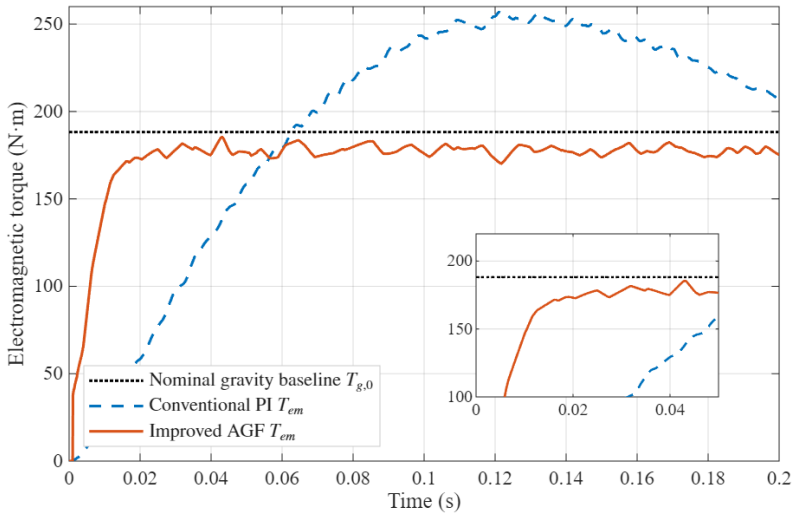


Figure 9: Electromagnetic torque responses during heavy-load start-up under the extreme suspended full-load condition ($m = 4.8$ t).

To quantitatively evaluate the initial torque-establishment performance, two indices are introduced with respect to the controller-side gravity-torque baseline $T_{g,0} = 188.2\ \mathrm{N \cdot m}$. The first index is the time required for the electromagnetic torque to reach 90% of $T_{g,0}$, defined as

$$t_{90} = \min\left\{ t \geq 0 \;\middle|\; T_{\mathrm{em}}(t) \geq 0.9 T_{g,0} \right\}. \tag{27}$$

Accordingly, the torque threshold is $0.9T_{g,0} = 169.38\ \mathrm{N \cdot m}$. The threshold-crossing time is determined by linear interpolation between two adjacent simulation samples.

The second index is the average positive torque deficit during the first 50 ms of start-up, defined as

$$\overline{\Delta T}_{50} = \frac{1}{t_{50}} \int_0^{t_{50}} \max\left[0,\ T_{g,0} - T_{\mathrm{em}}(t)\right] \mathrm{d}t, \qquad t_{50} = 0.05\ \mathrm{s}. \tag{28}$$

The positive-part operation in Eq. (28) ensures that torque exceeding the gravity-torque baseline does not offset the preceding torque deficit. Therefore, a smaller value of $\overline{\Delta T}_{50}$ indicates faster and more sufficient establishment of the initial supporting torque.

As summarized in Table 3, the improved AGF reaches 90% of the controller-side gravity-torque baseline at 12.17 ms, whereas the conventional cascaded PI controller first reaches the same threshold at 52.93 ms. Thus, the improved AGF shortens t_{90} by approximately 77.0%. In addition, the average torque deficit during the first 50 ms decreases from 111.80 N · m under conventional PI control to 32.83 N · m under the improved AGF, corresponding to a reduction of approximately 70.6%. These quantitative results confirm that the improved AGF establishes the supporting electromagnetic torque substantially earlier and reduces the initial torque deficit responsible for load rollback.

Table 3: Quantitative comparison of the initial torque-establishment performance under the 4.8 t full-load condition.

Control Strategy	t_{90} (ms)	$\overline{\Delta T}_{50}$ (N · m)
Conventional cascaded PI	52.93	111.80
Improved AGF	12.17	32.83

To supplement the waveform comparisons with quantitative indices, the rollback error is defined as

$$e_{\mathrm{rb}}(t) = \max\bigl(0, -s(t)\bigr). \tag{29}$$

where $e_{\mathrm{rb}}(t)$ denotes the rollback error. The integral absolute rollback error is calculated as

$$\mathrm{IAE}_{\mathrm{rb}} = \int_0^{t_f} e_{\mathrm{rb}}(t)\mathrm{d}t, \qquad t_f = 0.2\ \mathrm{s}. \tag{30}$$

where t_f is the end of the evaluated start-up interval, and $\mathrm{IAE}_{\mathrm{rb}}$ represents the accumulated rollback error over this interval.

The rollback recovery time is defined as the first time at which the load displacement returns to zero after reaching its minimum value. Fig. 10 summarizes the main quantitative indices for the 4.8 t full-load condition.

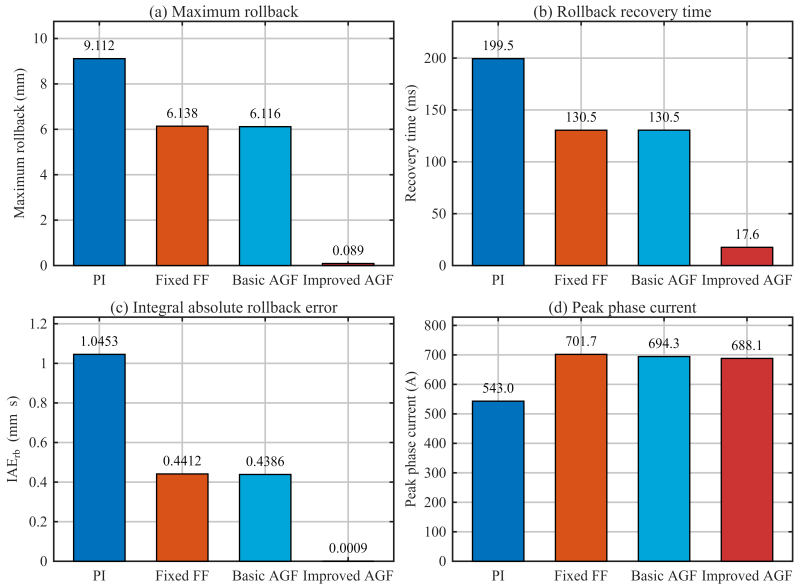


Figure 10: Quantitative comparison of the main start-up indices under the 4.8 t full-load condition: (**a**) maximum rollback; (**b**) rollback recovery time; (**c**) integral absolute rollback error; and (**d**) peak phase current.

Compared with conventional PI control, the improved AGF reduces the maximum rollback from 9.1124 mm to 0.0894 mm and the recovery time from 199.48 ms to 17.57 ms. Its $\mathrm{IAE}_{\mathrm{rb}}$ is 0.000905 mm · s, while the peak phase current is 688.08 A. These results indicate that the principal benefit of the improved AGF lies in stronger rollback suppression and faster recovery, while its peak phase current remains comparable to those of the other feedforward strategies.

To evaluate the influence of plant-side motor rotor-inertia variation, the motor rotor inertia J_m is set to $0.8J_{m,\mathrm{nom}}$, $1.0J_{m,\mathrm{nom}}$, and $1.2J_{m,\mathrm{nom}}$, while the controller-side inertia estimate $\hat{J}_{eq}$ and all other independently specified plant and controller parameters are kept at their nominal settings. According to Eq. (2), varying J_m produces a corresponding change in the actual plant-side equivalent total inertia J_{eq}. The minimum load displacement within 0–0.2 s is used to characterize the initial rollback response.

As shown in Fig. 11, the minimum load displacements are −0.1155 mm, −0.0894 mm, and −0.0728 mm when the motor rotor inertia is $0.8J_{m,\mathrm{nom}}$, $1.0J_{m,\mathrm{nom}}$, and $1.2J_{m,\mathrm{nom}}$, respectively. A reduction in rotor inertia produces a slightly larger initial rollback, whereas an increase in rotor inertia reduces the reverse

displacement. Despite these differences, all three cases recover to forward displacement after the initial transient, and the displacement responses remain close over the tested range. These results indicate limited sensitivity to the tested motor rotor-inertia variation.

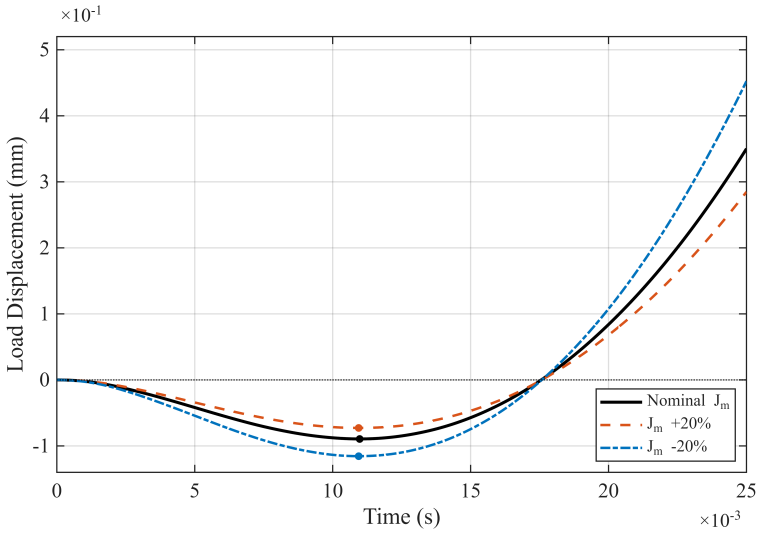


Figure 11: Load-displacement responses under motor rotor-inertia variations.

To further evaluate parameter sensitivity, two sets of cases were considered. In the friction-parameter cases, T_c and T_{st} were scaled together by ±20%, while the remaining plant and controller parameters were kept at their nominal values. In the inertia-estimation-error cases, only the controller-side estimate $\hat{J}_{eq}$ used in Eq. (13) was varied by ±20%, while the plant parameters remained unchanged. Since mechanical wear develops much more slowly than a single start-up transient, the friction-parameter offsets were held constant within each simulation.

As summarized in Table 4, the maximum absolute deviations from the nominal case in maximum rollback, rollback recovery time, and peak phase current are approximately 1.14%, 4.54%, and 0.46%, respectively. Friction-parameter variations produce only minor changes in the selected start-up indices. Underestimating $\hat{J}_{eq}$ slightly increases the rollback and rollback recovery time, whereas overestimating it slightly reduces both. As expected from Eq. (13), the peak inertia-feedforward torque varies proportionally with $\hat{J}_{eq}$. Overall, the selected start-up indices show limited variation within the tested parameter range.

Table 4: Sensitivity of start-up performance to friction-parameter variation and inertia-estimation error.

Case	Max. Rollback (mm)	Recovery Time (ms)	Peak Phase Current (A)	Peak T_I (N·m)
Nominal	0.08938	17.565	688.08	4.834
Friction − 20%	0.08967	17.585	685.96	4.834
Friction + 20%	0.08909	17.550	684.93	4.834
$\hat{J}_{eq}$ − 20%	0.09040	18.363	689.22	3.867
$\hat{J}_{eq}$ + 20%	0.08867	16.957	689.78	5.801

4.6 Effect of the Low-Pass-Filter Cutoff Frequency

To further evaluate the influence of the filter-induced phase lag on the initial start-up dynamics, additional simulations were conducted using nominal cutoff frequencies of 100, 200, and 400 Hz. The

electrical and mechanical parameters, feedback-controller gains, sampling periods, and operating conditions were kept unchanged, and only the cutoff frequency of the composite-feedforward filter was varied. Since the differences among the filtered torque responses are mainly concentrated in the initial stage, the first 10 ms of the start-up process is considered.

As shown in Fig. 12, the phase lag introduced by the low-pass filter is manifested in the time domain as a delayed buildup of the composite feedforward torque. The 100 Hz filter produces the slowest response, whereas the 400 Hz filter provides the fastest initial buildup but exhibits a short transient overshoot. The nominal 200 Hz case presents an intermediate response and approaches the raw composite feedforward torque without the pronounced initial overshoot observed in the 400 Hz case.

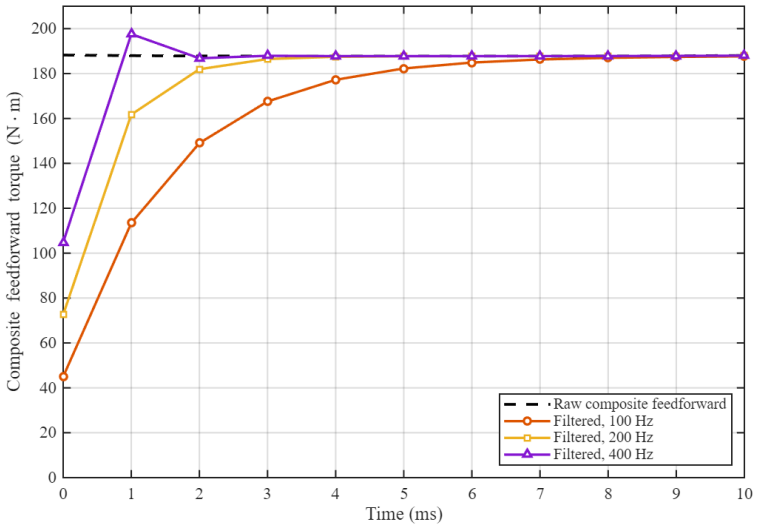


Figure 12: Initial buildup of the raw and filtered composite feedforward torques under different nominal cutoff frequencies during the first 10 ms of start-up.

The maximum difference among the three filtered torque responses is approximately 84.16 N · m at 1 ms. This difference decreases rapidly to approximately 5.50 N · m at 5 ms, 1.50 N · m at 7 ms, and 0.30 N · m at 10 ms. Therefore, the differences caused by the cutoff frequency are mainly concentrated in the first several milliseconds of the composite-feedforward-torque buildup. To estimate the mechanical effect within one control interval, the additional load-side displacement increment caused by the maximum inter-case torque difference is approximated as

$$\Delta s_{\text{step}} \approx \frac{R}{i} \frac{\Delta T_{FF,\max}}{2J_{\text{eq}}} T_s^2, \tag{31}$$

where $\Delta T_{FF,\max}$ is the maximum difference among the filtered feedforward torques. By conservatively assuming that $\Delta T_{FF,\max} = 84.16\ \text{N} \cdot \text{m}$ persists over one control interval of $T_s = 1$ ms, the estimated load-side displacement increment is

$$\Delta s_{\text{step}} \approx 0.00084\ \text{mm}. \tag{32}$$

This calculation shows that, within one control interval, the maximum torque difference among the three cutoff-frequency cases corresponds to a load-side displacement increment of 0.00084 mm, indicating a small local mechanical effect. This value represents the displacement increment caused by the maximum

torque difference over a single control interval. Therefore, the nominal cutoff frequency of 200 Hz is retained as a compromise between rapid compensation-torque buildup and suppression of an excessive discrete transient response.

5 Conclusions

This paper investigated the heavy-load start-up transient of an IPMSM-driven gravity energy storage system (GESS) hoisting unit and developed a torque-balance-based adaptive gravity feedforward (AGF) compensation framework. The main conclusions are as follows:

1. Under the extreme suspended full-load condition ($m = 4.8$ t), conventional cascaded PI control produces a maximum start-up rollback of 9.1124 mm because of delayed torque buildup. Fixed gravity feedforward reduces the maximum rollback to 6.138 mm, but introduces a pronounced transient current peak and stronger low-speed current oscillation.
2. Under the half-load condition ($m = 2.4$ t), the fixed feedforward torque tuned for full load produces overcompensation. The basic AGF updates the gravity compensation baseline according to the current load mass and slope angle, verifying the variable-load adaptability of adaptive gravity reconstruction.
3. Under the 4.8 t full-load condition, the improved AGF reduces the maximum rollback to 0.0894 mm and restores positive displacement earlier than the basic AGF. It also enables the phase current to enter a stable periodic state earlier, indicating stronger rollback suppression and a smoother low-speed current response.
4. When the motor rotor inertia J_m is varied by ±20% around its nominal value, the minimum load displacement ranges from −0.1155 mm to −0.0728 mm, and all investigated cases recover to forward displacement after the initial transient. These results indicate satisfactory start-up behavior over the tested rotor-inertia range.

Overall, under the investigated upward heavy-load start-up condition, the proposed framework improves the displacement response, current smoothness, and load adaptability of the IPMSM-driven GESS hoisting unit and maintains satisfactory start-up behavior under the tested parameter variations, without changing the basic hardware topology.

Future work will focus on establishing a hardware experimental platform to validate the proposed adaptive gravity feedforward (AGF) control framework and to further examine its practical implementation. Particular attention should be given to the reliable online acquisition or estimation of key operating information, including the load mass, track slope, effective transmission efficiency, and dominant friction parameters, together with validity monitoring and bounded parameter updating. Hardware implementation should also consider coordinated current limiting and software–hardware overcurrent protection, as well as safe bumpless transition between the normal AGF mode and a bounded fallback mode. The framework may also be extended to regenerative lowering and bidirectional operation and compared with representative observer-based and robust control methods under consistent operating conditions and evaluation criteria.

Acknowledgement: Not applicable.

Funding Statement: This research was funded by the Gansu Provincial Key Research and Development Program (Industrial Field), grant number 26YFGA027; and the Gansu Provincial Natural Science Foundation, grant number 23JRRA841.

Author Contributions: The authors confirm contribution to the paper as follows: Conceptualization, Zheng Cao and Wei Li; methodology, Zheng Cao and Wei Li; software, Wei Li; validation, Wei Li and Teng Li; formal analysis, Wei

Li; investigation, Wei Li and Teng Li; resources, Zheng Cao; data curation, Wei Li; writing—original draft preparation, Wei Li; writing—review and editing, Zheng Cao, Wei Li and Teng Li; visualization, Wei Li; supervision, Zheng Cao; project administration, Zheng Cao; funding acquisition, Zheng Cao. All authors reviewed and approved the final version of the manuscript.

Availability of Data and Materials: The simulation parameters supporting the findings of this study are provided within the article. The processed MATLAB simulation data used to generate the main figures, including load displacement, inverter three-phase current, and estimated electromagnetic torque data, are available in the Supplementary Materials. Additional MATLAB/Simulink files are available from the corresponding author upon reasonable request.

Ethics Approval: Not applicable.

Conflicts of Interest: The authors declare no conflicts of interest to report regarding the present study. The funders had no role in the design of the study; in the collection, analyses, or interpretation of data; in the writing of the manuscript; or in the decision to publish the results.

Supplementary Materials: The supplementary material is available online at https://www.techscience.com/doi/10.32604/ee.2026.085812/s1. The supplementary material includes processed MATLAB simulation data used to generate the main simulation figures, together with a README file describing the data structure, variable names, and units.

References

1. Cai K, Han Y, Xia R, Wu J, Wang J, Lund PD. Gravity energy storage: a review on system types, techno-economic assessment and integration with renewable energy. Wiley Interdiscip Rev Energy Environ. 2024;13(6):e543. [CrossRef]
2. Hunt JD, Zakeri B, Falchetta G, Nascimento A, Wada Y, Riahi K. Mountain Gravity Energy Storage: a new solution for closing the gap between existing short- and long-term storage technologies. Energy. 2020;190:116419. [CrossRef]
3. Wang X, Yang H, Li X, Deng Z, Fu G, Wu Q, et al. Gravitational energy storage: media taxonomy, efficiency factors, comparison and selection. Appl Energy. 2025;395:126233. [CrossRef]
4. Tong W, Lu Z, Hunt JD, Zhao H, Zhao G, Han M. Power control strategies for modular-gravity energy storage plant. Appl Energy. 2024;361:122908. [CrossRef]
5. Tong W, Lu Z, Hunt JD, Zhao H, Han M, Zhao G. Energy management system for modular-gravity energy storage plant. J Energy Storage. 2023;74:109283. [CrossRef]
6. Hulak D, Remiorz L. Analysis of gravity energy storage management methods for power stability. J Energy Storage. 2025;139:118852. [CrossRef]
7. Wang G, Yang R, Xu D. DSP-based control of sensorless IPMSM drives for wide-speed-range operation. IEEE Trans Ind Electron. 2013;60(2):720–7. [CrossRef]
8. Li X, Yin Y, Zhou Y, Liu W, Zhao K. The non-singular fast terminal sliding mode control of interior permanent magnet synchronous motor based on deep flux weakening switching point tracking. Energ Eng. 2023;120(2):277–97. [CrossRef]
9. Sawma J, Seferian V, Khatounian F, Monmasson E, Ghosn R. An improved anti-rollback control algorithm for gearless traction motor in elevator applications. Mechatronics. 2021;79:102659. [CrossRef]
10. Gil J, You S, Lee Y, Kim W. Nonlinear sliding mode controller using disturbance observer for permanent magnet synchronous motors under disturbance. Expert Syst Appl. 2023;214:119085. [CrossRef]
11. Cupertino F, Naso D, Mininno E, Turchiano B. Sliding-mode control with double boundary layer for robust compensation of payload mass and friction in linear motors. IEEE Trans Ind Appl. 2009;45(5):1688–96. [CrossRef]
12. Zhang J, Li J, Ren W, Sun XM. Nonlinear speed-tracking control with overcurrent protection for uncertain permanent magnet synchronous motor systems. Trans Inst Meas Control. 2024;46(4):666–77. [CrossRef]
13. Li J, Zhang L, Luo L, Li S. Extended state observer based current-constrained controller for a PMSM system in presence of disturbances: design, analysis and experiments. Control Eng Pract. 2023;132:105412. [CrossRef]

14. Zhang Z, Chen Z, Li N, Chen K, Cheung NC, Pan J. A dynamic convergence second-order sliding mode control structure for PMSM with an observer based on a novel sliding mode reaching law. Control Eng Pract. 2025;164:106504. [CrossRef]
15. Rigatos GG, Abbaszadeh M, Marignetti F, Siano P. A nonlinear optimal control approach for voltage source inverter-fed three-phase PMSMs. COMPEL Int J Comput Math Electr Electron Eng. 2023;42(6):1690–717. [CrossRef]
16. Wang C, Peng J, Pan J. A novel friction compensation method based on Stribeck model with fuzzy filter for PMSM servo systems. IEEE Trans Ind Electron. 2023;70(12):12124–33. [CrossRef]
17. Zhang W, Li M, Gao Y, Chen YQ. Periodic adaptive learning control of PMSM servo system with LuGre model-based friction compensation. Mech Mach Theory. 2022;167:104561. [CrossRef]
18. Xu R, Zhou M. Sliding mode control with sigmoid function for the motion tracking control of the piezo-actuated stages. Electron Lett. 2017;53(2):75–77. [CrossRef]
19. Younesi A, Kazemi Y, Moradpour A, Tohidi S. Optimized sensor and sensorless control of PMSM modeled in discrete mode: a comparison of KH and PSO algorithms. COMPEL Int J Comput Math Electr Electron Eng. 2016;35(3):1293–320. [CrossRef]